Optical and transport properties of ultrathin NbN films and nanostructures

Semenov, A ; Günther, B ; Böttger, U ; Hübers, H W ; Bartolf, H ; Engel, A ; Schilling, A ; Ilin, K ; Siegel, M ; Schneider, R ; Gerthsen, D ; Gippius, N A

DOI: https://doi.org/10.1103/PhysRevB.80.054510

OPTICAL AND TRANSPORT PROPERTIES OF ULTRA-THIN NbN FILMS AND NANOSTRUCTURES

A. Semenov, B. Günther, U. Böttger, H.-W. Hübers
DLR Institute of Planetary Research, Rutherfordstrasse 2, 12489 Berlin, Germany
H. Bartolf, A. Engel, A. Schilling
Physics-Institute, University of Zürich, Winterthurerstrasse 190, 8057 Zürich, Switzerland
K. Ilin, M. Siegel
Institute of Micro- und Nano-electronic Systems, University of Karlsruhe, Hertzstrasse 16, D-76187 Karlsruhe, Germany
R. Schneider, D. Gerthsen
Laboratory for Electron Microscopy, University of Karlsruhe, D-76128 Karlsruhe, Germany
N.A. Gippius
LASMEA, UMR 6602 CNRS, Université Blaise Pascal, 63177 Aubière, France
and A.M.Prokhorov General Physics Institute, Russian Academy of Sciences, Moscow 119991, Russia

Abstract
Optical and transport properties of a series of ultra-thin NbN films with different thickness grown on sapphire have been evaluated by means of spectral ellipsometry and dc measurements of superconducting critical parameters. The growth process and thus the nitrogen content have been optimized for each film in the series to achieve the highest superconducting transition temperature, which however increases with the film thickness. Optical and transport measurements agree in slowly increasing disorder while the electron density of states at the Fermi level shows a twofold decrease when the film thickness drops from 14 to 3 nm. Near infrared extinction spectra of nanowire gratings from our films are well described by the scattering matrix method that uses optical parameters of non-structured films and the grating geometry. The technique provides an attractive tool for analyzing various devices for nano-photonics.

PACS: 74.25.Fy 74.78.Na 74.25.Nf

I. INTRODUCTION

Optical and near-infrared properties of ultra-thin superconducting NbN films and subwavelength gratings have attracted attention in the last several years due to their application for single photon detection [1]. The short coherence length of NbN (typically a few nanometers) makes it possible to fabricate nanometer thick superconducting films with a transition temperature above 10 K. Although epitaxial NbN films can be grown on a variety of substrates [2, 3, 4], e.g. Si, MgO, or Al_2O_3, with a few exceptions [4] nanometer thick films typically have either amorphous or polycrystalline twinned structure [5]. Controlling the crystalline structure is getting more difficult as films become thinner. Standard techniques, such as x-ray scattering and reflectance loose their accuracy due to the decreasing sensitivity. Optical measurements may provide an alternative way. For example, the permittivity spectra near the plasma edge can be used for phase identification in NbN films [6]. To some extent the already existing knowledge of superconducting and transport parameters of thick NbN films may help to optimize modern devices made from ultra-thin films. It has been shown [7] that in relatively thick films a deviation from the optimal growth conditions and stoichiometry affects the transition temperature via a decreasing density of electronic states and, consequently, carrier density. The degradation of superconductivity with the decrease of the film thickness even at optimal growth conditions makes it important to study transport

parameters directly in those ultra-thin films, which are used for device fabrication. Transport properties (e.g. electron scattering rates) extracted from near-infrared [6] and infrared spectra [8] may differ substantially even for relatively thick films. The issue is obviously more crucial for thin films suffering from structural defects, oxidation and mechanical stress. Thus reliable determination of transport parameters for such films would require a combination of optical and conventional low-frequency methods. Electrodynamic properties of subwavelength gratings have been intensely studied for a long time, first in the terahertz range and recently also in the near infrared. These studies were driven by applications for beam handling techniques where the absorbance deteriorates the grating performance and has to be minimized. Not so much attention has been paid to possible ways of maximizing the absorbance of the grating that is the key issue in the detector application.

In this paper we report on optical and transport properties of nanometer thick superconducting NbN films on sapphire. We evaluate by means of ellipsometry optical constants and electron scattering rates in non-structured films with different thicknesses and then extract transport parameters such as electron diffusivity and density of electron states from their superconducting properties: transition temperature, critical magnetic field and current. Combining optical and transport data we model the optical properties of nanowire gratings made from ultra-thin NbN films. We finally compare the modeled extinction spectra with the experimentally measured polarization sensitivity of nanowire single-photon detectors. The paper is organized as follows: Section II briefly describes the formalism which was used to extract transport parameters from optical and superconducting properties while mathematical details are presented in the appendix. The next section contains experimental data and the evaluation of transport parameters for NbN films with thicknesses varying from 3 to 14 nm. The last section is devoted to optical properties of nanowire gratings, specifically to their absorbance and extinction spectra.

II. FORMALISM

Since our NbN films most likely occupy an intermediate position between good metals like gold or aluminum and a semiconductor, the permittivity for a film with known thickness was determined as the complex spectral function that provided the best fit to the data of ellipsometry measurements. In general the permittivity of a metal can be presented as a function of the circular frequency ω in the following form

$$\varepsilon_r = \varepsilon_{r0} - \frac{\omega_p^2}{\omega\left(\omega + j\frac{1}{\tau}\right)} + \sum_q \frac{\Omega_{Sq}^2}{\Omega_{0q}^2 - \omega^2 - \mathrm{j}\Omega_{Dq}\omega} \qquad (1)$$

with the permittivity at large frequencies ε_{r0}, the plasma frequency ω_p and the elastic electron scattering time τ, which we used as fitting parameters. Intraband transitions active in the ultraviolet and partly in the visible portion of the spectrum were modeled as a set ($q = 2$) of single oscillators each having its own strength Ω_{Sq}, central frequency Ω_{0q} and damping Ω_{Dq}. In the near-infrared portion of the spectrum the contributions of these oscillators to the total permittivity of a good metal should become negligible. We made sure that the thickness d of all studied films was much smaller than the electromagnetic skin depth in the visible and near-infrared that justified the use of the film impedance $Z_F = Z_0\, c\left(\omega d\, \varepsilon_r\right)^{-1}$ (here c is the velocity of light in vacuum and Z_0 the impedance of vacuum) for computing the absorbance of non-structured films. The absorbance as a function of the film impedance (Eq. A5) is

evaluated in the appendix. Although NbN is a strong-coupling superconductor, for the sake of clarity we will use the Bardeen-Cooper-Schrieffer (BCS) relation between the transition temperature and the energy gap. The impact of the possible variation of the coupling strength with the disorder will be discussed later in the section describing superconducting properties of our films. The analysis below uses as input data the temperature dependence of the critical current near the transition temperature in zero magnetic field and the resistive superconducting transitions at different magnetic fields perpendicular to the film surface. For each magnetic field, we considered the transition temperature at the upper critical magnetic field to be the temperature when the resistance dropped to half its normal state value. This, in turn, gives us the temperature dependence of the upper critical magnetic field $B_{C2}(T)$. The slope of this dependence in the vicinity of the superconducting transition temperature T_C allows one to evaluate the value of the critical field at zero temperature $B_{C2}(0)$ and the electron diffusivity. NbN films typically have rather small electron mean free paths (l) and relatively large magnetic penetration depths (Λ) obeying the relation $l << \xi_0 << \Lambda$ where ξ_0 is the BSC coherence length. This condition puts them in the limiting case of a dirty superconductor and local electrodynamics. In this case the diffusivity and the critical current density at zero temperature can be respectively expressed (see Appendix) in the following forms

$$D[\mathrm{cm^2 sec^{-1}}] = \frac{1.097}{\left[-\frac{dB_{C2}(T)}{dT}\right]_{T=T_C} [\mathrm{T K^{-1}}]} \qquad (2)$$

and

$$j_C(0)\left[\mathrm{MA\,cm^{-2}}\right] = 0.18\, N_0 \left[10^{47}\,\mathrm{J^{-1}\ m^{-3}}\right] (T_C[\mathrm{K}])^{\frac{3}{2}} \left(D\left[\mathrm{cm^2\,sec^{-1}}\right]\right)^{\frac{1}{2}}, \qquad (3)$$

where N_0 is the density of electronic states per one spin at Fermi level. The critical current density at zero temperature was obtained by fitting the experimental critical current density j_C near the transition temperature with the two-fluid temperature dependence of the depairing critical current density $j_C(T) = j_C(0)(1-t^2)(1-t^4)^{1/2}$, where $t = T/T_C$. The density of states was determined by means of the relation above from the values of the electron diffusivity, transition temperature and the critical current density at zero temperature.

III. EXPERIMENTAL DATA

A. Film and sample preparation

Superconducting NbN films were grown at a rate of $0.17\,\mathrm{nm\,sec^{-1}}$ on the optically polished side of R-plane sapphire substrates by means of DC reactive magnetron sputtering of a pure Nb target in an Ar+$\mathrm{N_2}$ gas mixture. The rear sides of the substrates were ground in order to eliminate back reflection. The deposition process was optimized with respect to the partial pressure of $\mathrm{N_2}$ and the deposition rate to provide the highest transition temperature for films with the smallest studied thickness. More details on the film deposition are reported in Ref. 9. We verified that the optimal set of deposition parameters remained unchanged for films

thinner than 15 nm. Superconducting properties were measured on narrow stripes which were produced from freshly deposited films by means of electron-beam lithography and ion milling technique. Stripes typically containing 10 squares (the length of the strip amounted ten times the strip length) had widths between 5 and $10\,\mu m$ and six contacts for conductivity and Hall measurements. We note that the difference between superconducting transition temperatures of stripes wider than 1 μm and non-structured films was always less than 0.5 K but amounts to 1 to 2 K for strips with a width less than 100 nm [10]. Optical measurements were performed on gratings made from 50 to 100-nm wide strips [11]. Strips were connected at the grating edges (Fig. 1b) to form a continuous meandering line.

The major goal of the study was to find variations of transport parameters with the film thickness; therefore a lot of effort was put into an accurate definition of the film thickness. We evaluated the thickness by combining different measurement techniques. We used high-resolution transmission electron microscopy (HRTEM) in a 200 kV TEM Philips CM 200 equipped with a field-emission gun, atomic force microscopy (AFM) and glancing incidence X-ray reflection [5]. As an example a cross-section HRTEM image of the film/substrate interface is shown in Fig. 1a along with the AFM picture (Fig. 1b) of the meander line in top view made from the reference film. Owing to the procedure used to prepare cross-section specimens for TEM, in Fig. 1a the NbN layer is covered with carbon. Films with optimal Nb-N composition (δ -NbN phase) have a face-centered cubic (fcc) structure with a lattice constant of 0.44 nm. From the HRTEM micrograph we conclude that the NbN layer consists of nanocrystallites and has a mean thickness of 5 nm. Because of the presence of these crystallites and their different orientations relative to the underlying Al_2O_3 substrate, the surface of the NbN film appears to be relatively rough. Moreover, the image contrast of the topmost regions of the NbN crystallites (namely a missing periodicity that can only hardly be recognized due to the Carbon cap layer, indicating an amorphous structure) hints to an approximately 1 nm thick oxide layer. Such thin Nb oxides on top of NbN layers were already detected for NbN layers on silicon [12]. The AFM profile taken across the meander lines confirms a total film thickness (NbN plus oxide) of $\approx$ 6 nm. It also shows that the variation of the film thickness between lines is less than 1 nm. X-ray examination revealed for the reference film a total thickness of 5.3 nm and an approximately 0.7 nm thick oxide layer on top of NbN film. Thus all techniques agree in the same film thickness with an accuracy of two atomic layers (0.8 nm). Analysis of the AFM picture of the 160-nm wide meander line shows that the variation of the line edge is below 10 nm making the accuracy of the width definition better than 12%. For measurements of transport and polarization properties we selected a few samples from a series of nominally identical structures aiming at the smallest resistance above the superconducting transition and the largest critical current density.

Both HRTEM and X-ray glancing reflectivity techniques indicated that there is always an oxide layer (presumably Nb_2O_5) on top of NbN films. This layer appears within a few minutes after exposing the film to air for the first time. The thickness of the oxide layer on newly prepared films varies in the range from 0.5 to 1 nm [13]. Further oxidation proceeds much slower. Since we did not measure the oxide layer thickness for all our films, we used the total thickness (NbN + Nb_2O_5) for the evaluation of the transport parameters. This might bring an uncertainty of approximately 15% to the values of transport parameters obtained in the present study.

Close to but above the superconducting transition temperature T_C we modeled the total resistivity of our films assuming two contributions: a constant normal-state conductivity σ_n and a contribution from superconducting fluctuations of the Aslamasov-Larkin (AL) type σ_{AL} [14]. The total resistivity then equals $\rho = 1/(\sigma_n + \sigma_{AL})$. For the temperature interval $0 < (T - T_C)/T_C < 0.15$ all of our films could be best fitted using the 2D-form for the AL

fluctuation conductivity $\sigma_{AL} = e^2 T_C (16\hbar d(T - T_C))^{-1}$. Besides a reliable determination of T_C by fitting this model to the experimental data, we also obtained the normal state resisitivity ρ_n close to T_C and an estimate of the film thickness d that is in rough agreement with the thickness determined by other methods. For higher temperatures we see systematic deviations from this 2D-model in films with $d \geq 10$ nm, which would be consistent with the temperature-dependent coherence length becoming smaller than the film thickness.
Values for T_C and ρ_n are summarized in Table 1 and 3 and plotted in Fig. 2 as a function of the film thickness. For comparison with the optical impedance we also computed the dc resistance of a film square $R_S = R(295)\, N^{-1}$ where $R(295)$ and N are the resistance of the strip at room temperature and the number of squares, respectively. Our results show the well known trend (see e.g. [2, 15]) that the transition temperature drops and the resistivity increases when the thickness decreases. The residual resistance ratio (RRR), that is the ratio of film square resistances at temperatures 295 K and 20 K, increases with the film thickness and becomes larger than one for films thicker than 14 nm thus indicating metallic behavior. All studied films and their transport properties are listed in Table 1. Samples #206 and #207 were grown with nitrogen deficiency that shifted them more towards the metallic phase [6, 7]. They both have smaller resistivity and larger electron diffusivity than one would expect for optimal NbN films of the same thicknesses. The RRR of these films is also higher than for films with optimal composition.

B. Optical properties of non-structured films

The optical properties of non-structured films were evaluated at room temperature using a spectroscopic ellipsometer SE 850 (SENTECH, Berlin, Germany) in the wavelength range 0.24 to 5 μm. The relative dielectric constants ε_r of a few films with different thicknesses are shown in Fig. 3. The long-wavelength portions of all plots are well described by the free electron (Drude) model (second term in Eq. 1) while features near the short-wavelength edge are most likely due to the band-gap effects in NbN. These features are well fitted with only one additional oscillator (third term in Eq. 1) having the same parameters for all studied films. As a consequence of the relatively low dc conductivity, all films demonstrate a non-vanishing real permittivity even at frequencies below the plasma frequency. To account for that, we had to introduce a second oscillator with film dependent parameters. Best fit parameters of the two oscillators are summarized in Table 2. We can not ascribe oscillator frequencies and strengths to any particular structure of the Fermi surface and will therefore not further discuss these fitting parameters. However, it is important to note that for all our films added oscillators changes the free-electron value of the permittivity at near infrared by less than 20%.
Parameters of the Drude model (plasma frequency and electron elastic scattering time) which provided the best fit to the long-wavelength range of the plots are listed in Table 1. The plasma frequency does not noticeably vary from film to film; its mean value corresponds to the wavelength 0.15 μm. Introducing into the film model a 2-nm thick layer of niobium dioxide NbO_2 (optical parameters of Nb_2O_5 are not known, we assume here that they do not significantly differ from the optical parameters of niobium dioxide), we found that best fit values of the electron scattering rate and the plasma frequency almost coincide with the best fit value obtained for the model without dioxide layer. The most pronounced changes (approximately 15%) of the best fit values were found for the thickest NbN film. Thus for the purpose of optical characterization the effect of the dioxide layer can be safely neglected, if the film thickness is less than 10 nm. For thin NbN films it has been shown [6] that changes in

the frequency dependence of the real part of the dielectric constant correlate well with the electronic structure of the film and that those correlations can be used for phase identification. The measured frequency dependence of the relative dielectric constant (Fig. 3) indicates that to the extent of the reliability of the method our films have the fcc δ-NbN structure. Using the dielectric constant and the film impedance approach, we computed the film absorbance that is shown in Fig. 4. The inset in Fig. 4 shows the real and imaginary parts of the impedance for the 5.6 nm thick film. This frequency dependence of the impedance was typical for all studied films.

Although optical properties of our films in the near-infrared are well described by the free electron (Drude) model the films are far from being in the limiting case of a good metal (see discussion in the appendix). The imaginary part of the film impedance remains noticeably large throughout the near-infrared spectral range and becomes negligible at wavelengths larger than several micrometers, only. We therefore chose the wavelength of $5\ \mu m$ for a comparison between the real part of the impedance and the dc square resistance of our films. The values of the real part of the impedance at this wavelength, denoted as $\mathrm{Re}(Z_F)$, are listed in Table 1. As one can see, the difference between the dc square resistance at room temperature and the real part of the impedance increases when films become thinner and reaches 30% for the 3.2 nm thick film. Correspondingly, absorbance in the near-infrared reaches the maximum for films with a thickness close to 8 nm. Such films have a dc square resistance (165Ω for the 8.3 nm thick film, Table 1) that is almost 20% larger than the value $\approx 140\Omega$ that maximizes the absorbance of a film from an ideal metal. We have to admit that more relevant for comparison with low temperature transport properties would be optical constants determined at low temperatures. However, one should not expect substantial difference between low and high temperature data at frequencies mach larger than the frequency corresponding to the superconducting energy gap.

C. Transport and superconducting properties

The temperature dependence of the upper critical magnetic field for stripes with different thicknesses is shown in Fig. 5. The solid lines are the linear fits to the measured temperature dependences. Taking into account that the Ginsburg-Landau (GL) model holds for dirty films at temperatures well below the transition temperature, we neglected for the thinnest films the nonlinear portion of the temperature dependences in the vicinity of T_C. The electron diffusion coefficients, which we obtained using Eq. 2, are listed in Table 1. The GL coherence length at zero temperature $\xi(0) = \Phi_0^{1/2}(2\pi B_{C2}(0))^{-1/2}$, where $\Phi_0 = \pi\hbar/e$ is the magnetic flux quantum and e is the electron charge (see Eq. A6 and discussion thereafter), does not systematically vary with the film thickness. The values for all samples fall in the range from 5 to 7 nm. The electron mean free path was calculated as $l = (3D\tau)^{1/2}$ where the electron scattering time τ was taken from the ellipsometry data. It shows that indeed the films are in the dirty limit $l << \xi(0)$.

We measured the critical current density using micrometer wide stripes. Near the transition temperature, the critical current density of all studied samples closely followed the two-fluid temperature dependence of the depairing critical current. Using the least-square fits to the experimental data in the temperature range above $0.85T_C$ and assuming uniform current distribution over the cross-section of the strips, we extractsd the depairing critical current densities at zero temperature, which are listed in Table 1. We shall note here that the calculated critical current density at $T = 0$ is a parameter that we were not able to achieve experimentally. The critical currents measured in liquid helium (4.2 K) for wide stripes ($w > 3\mu m$) were already systematically lower than the current predicted by Eq. 3. We assume

that magnetic vortices entering the stripe due to the magnetic self-field define the critical state at low temperatures and prohibit measurements of the true depairing critical current [16]. Another reason for the deviation at low temperatures could be the decrease of the GL coherence length that becomes comparable with the film thickness thus breaking the validity of the GL model with the constant order parameter. The critical current density at zero temperature ranged from approximately 3×10^6 to 1.3×10^7 A cm^{-2} for film thicknesses from 3 to 14 nm, respectively.

The most important material parameter for single-photon detector applications is the electron density of states at the Fermi level. This quantity, together with the superconducting energy gap Δ, defines the density of the free energy difference between the superconducting and normal state $\Delta F = (1/2) N_0 \Delta^2$ and thus the volume in which an absorbed photon with a particular energy is able to destroy superconductivity. The density of electronic states computed with Eq. 3 is shown in Fig. 6 as a function of film thickness. For films with a thickness larger than 8 nm the density of states remains constant and coincides with the density of states reported for a thick (50 nm) NbN film with the same stoichiometry [7]. At smaller thicknesses the density of states decreases and for our thinnest measured films drops to less than one half of the thick-film value. Taking into account the strong coupling correction for the energy gap $2\Delta(0) = 4.15 k_B T_C$ that was experimentally found for single-crystal 200-nm thick NbN films on magnesium oxide [2] as well as for 10 to 5 nm thick stoichiometric NbN films on sapphire [17], one would conclude a 1.3 times smaller value for the density of states. These corrected values coincide within 20% accuracy with the density of states per electron spin obtained from the free electron relation $N_0 = (2 e \rho_n D)^{-1}$, if one takes the experimental values of the electron diffusivity and resistivity in our films. We shall note that the coincidence between the densities of states found via critical current and via resistivity indirectly evidences the high homogeneity of our nanostripes. Indeed, a few constrictions in a long wire would not noticeably modify the resistivity, but would drastically reduce the measured critical current. At this stage we can not justify that the strong coupling correction remains unchanged also for films thinner than 5 nm. The reduction of the density of states together with an increasing degree of disorder may change the coupling scenario in thin films as it happens in strongly disordered thick films [18]. We note, however, that the Ioffe-Regel parameter, which we computed in the framework of the free electron model as $k_F l = \hbar (3\pi^2)^{2/3} n_e^{-1/3} (e^2 \rho_n)^{-1}$ where n_e is the free electron concentration, varies from 2.6 to 5.6 (see Table 3) in the range of film thicknesses covered in this study. Hence the expected variation of the transition temperature and the density of states due to disorder [7, 18] is less than we have observed in our films. The most probable reason for enhanced decrease of these parameters with decreasing the film thickness is the proximity effect with the oxide layers on both surfaces of ultra thin films [12].

For three films with different thicknesses, which were deposited in a different run similarly to those used for transport studies, we have also measured the Hall-voltage for magnetic inductions between -6 and +6 T. For Hall-voltage measurements we chose a relatively large excitation current of 0.5 mA. The experimental results as a function of magnetic induction measured at 50 K are shown in Fig. 7. The derived Hall constants and free carrier concentrations are summarized in Tab.3. We found the free electron concentration to vary between 1.26 and 2.6×10^{29} m^{-3}. The free-electron concentrations in the 6 and 12 nm thick films are in line with values obtained by another group in thicker NbN films with optimal nitrogen content and slightly larger superconducting transition temperature [7]. The increased charge-carrier concentration in the 3.2 nm thin film could be caused by interface or surface layers with significantly higher carrier concentrations.

On the other hand, the carrier concentration $\approx 5.5\times10^{28}$ m^{-3}, that we computed for our films

from the plasma frequency as $n_e = \omega_p^2 m_e \varepsilon_0 e^{-2}$ (see Table 1) with the assumption that the effective electron mass equals the free electron mass $m_e = m_0$, is noticeably lower than the Hall concentration. The difference between Hall concentration and the concentration extracted from the plasma frequency has been also observed for thicker NbN films [6]. The reason for the discrepancy is not clear. However, we note that assuming a lower effective electron mass, as it is expected in nitrides [19], would increase the discrepancy. Theoretical estimates of the free electron concentration in NbN vary from 2.39×10^{29} m^{-3} [20] to 9.2×10^{28} m^{-3} [6] depending on the accepted model of the conduction band. We note that our concentration values extracted from Hall measurements are all falling in this range.

IV. OPTICAL PROPERTIES OF NANOWIRE GRATINGS

We studied gratings built up from meandering narrow lines that covered an area of $4\times4\,\mu\text{m}^2$ with different filling factors. Similar structures have been recently demonstrated to be excellent single-photon detectors [21]. The absorbance of the grating can be analytically evaluated for an infinitely large structure in the limiting cases $\lambda >> w,P$ or $\lambda << w,P$, where λ is the wavelength in free space and w and P is the width and the pitch (period) of the grating, respectively. In the latter case, the absorbance of the grating for normal incidence does not depend on the polarization and equals the absorbance of the non-structured film times the grating filling factor $f = w\,P^{-1}$. For a sub-wavelength grating, i.e. for $\lambda >> w,P$, the absorbance of the grating can be obtained in the framework of the impedance formalism where the grating is considered as a birefringence layer [22] with the effective permittivity $\varepsilon_P = 1 + f(\varepsilon_r - 1)$ and $\varepsilon_S = [1 + f(\varepsilon_r^{-1} - 1)]^{-1}$ for light polarized parallel and perpendicular to the wires, respectively. To evaluate the absorbance in the intermediate wavelength range, we computed the absorbance of infinite planar gratings using the scattering matrix technique and assuming that the nanowires in the grating have the same permittivity as non-structured NbN films. The S-matrix technique [23] is particularly effective for gratings from dirty metals since the numeric result converges to the exact solution for a small number of Bragg harmonics thus making the computation extremely fast. Fig. 8 shows thus computed absorbance of the gratings with different filling factors for light polarized parallel and perpendicular to the grating wires. For both polarizations, the grating absorbance is a monotonously increasing function of the filling factor. Contrary, the extinction ratio, that is the ratio of absorbance values for two polarizations, decreases as the filling factor increases. This finding indicates that in detector applications the polarization sensitivity may be improved at least at the expense of the quantum efficiency. In a finite meander structure with the size comparable to the wavelength, edge effects should play a substantial role damping the extinction ratio. To account for that one has to implement the finite element technique. We ran the electrodynamics-problem-solver FEKO (EM Software & Systems-S.A. (Pty) Ltd.) to model the extinction ratio for our $4\times4\,\mu\text{m}^2$ meander structure. In this simulation we neglected the frequency dependence of the NbN permittivity and assigned to the meander material the constant square resistance. This resistance was chosen equal to the real part of the film impedance $\text{Re}(Z_F)$ optically measured for non-structured film at a wavelength above $5\,\mu\text{m}$. We made sure that the software provided the correct absorbance for the unstructured film as well as for the two limiting cases discussed above in connection with the analytical approach. To obtain the absorbance, the computed absorbed power was normalized to the power flux falling on the geometric area of the meander.

Direct experimental verification of the grating absorbance at normal incidence requires either enormously large gratings or has to cope with uncertainties arising from the non-uniform

intensity distribution in the focused beam. Here we used the meandering wire grid as a single-photon detector and compared the detection quantum efficiency for different light polarizations. It has been shown by our group [24] as well as by other groups [1, 25] that the sub-critically current-biased meandering wire grating is capable of counting single photons with polarization dependent quantum efficiency. The quantum efficiency is a product of the structure absorbance and the intrinsic quantum efficiency; the latter is believed to be polarization independent. The experimental setup is described elsewhere [26]. Briefly, the meander was cooled to 5 K and biased with the dc current $I = 0.9\,I_C$, where I_C is the critical current at this temperature. The grating was then exposed to light from an arc lamp passed through a prism monochromator. The light after the monochromator was expanded to form a spot much larger than the grating area, thus assuring uniform illumination of the grating with plane waves at normal incidence. The polarizer with an extinction ratio better than 10^3 was positioned in front of the grating. We measured the ratio of photon count rates and compared it with the computed absorbance ratio for the two orthogonal polarizations parallel and perpendicular to the meander wires. The result is shown in Fig. 9 for two gratings with $w = 90\,\text{nm}$, $f = 50\%$ and $w = 80\,\text{nm}$, $f = 47\%$ made from 4.8 and 4.3-nm thick films, respectively. Solid lines show the result of the FEKO simulation. The absorbance extinction ratio that we computed using the analytical birefringence approach [22] exceeded the measured extinction ratio by more than ten times and is not shown in Fig. 9. The extinction ratio obtained with the S-matrix technique was only slightly larger than values shown in Fig. 9. However, the absorbance provided by both the birefringence model and the S-matrix technique for P-polarization was close to the result of the FEKO simulations. By contrast, the absorbance for S-polarization obtained analytically was much lower than the S-polarization absorbance computed with both the S-matrix technique and FEKO. It has been already reported [27] that the birefringence approach might not be very accurate for metallic gratings. On the other hand, the coincidence between FEKO-simulated and measured extinction ratios is reasonably good, thus justifying the approach which we used for the optical characterization of sub-wavelength gratings. The deviation of the measured extinction ratio from the modeled ratio at large wavelengths was most likely caused by absorption of light in the contact pads that were not included in the simulation. We shall note that we could not experimentally attain a higher extinction ratio that is expected for gratings with low filling factor and narrower wires. The understanding of the reason, which is not clear at this time, requires further investigations. We speculate that the non-homogeneity of the wire edge occurring at the same scale as the non-uniformity of the electric field in the S-polarization may lead to plasmonic resonances that strongly modify the effective permittivity and thus enhance the absorbance in the grating wires.

V. CONCLUSION

We have explored optical and transport properties of ultra-thin superconducting NbN films on sapphire and nanowire gratings fabricated from these films as well as variations of these properties with the film thickness. Although there is a correlation between transport and optical data we have found systematic differences in the carrier concentration extracted from optical and transport measurements. The central observation of this paper is that for films with optimal composition the density of electronic states at the Fermi level decreases with the film thickness, while the carrier concentration and degree of disorder does not vary significantly. This fact brings us to the conclusion that in ultra-thin films with optimal composition the decrease of the transition temperature is jointly driven by the proximity effect and increasing disorder. The near-infrared properties of ultra-thin films are well described by the Drude model; however the films are far from being a good metal and exhibit a relatively large absorption. Another finding of the paper is that the polarization sensitivity of nanowire

single-photon detectors in the near-infrared is almost entirely defined by the optical constants of NbN films and the grating geometry while the detection mechanism remains polarization independent.

Acknowledgment

H.B. acknowledges support by the Swiss NCCR Manep. N.G. acknowledges support by Russian Foundation for Basic Research and by ANR Chair of Excellence Program. Authors are grateful to J.-C- Villégier for providing X-ray data and to A. Palladino for reading the manuscript.

APPENDIX: Evaluation of optical and transport parameters

A. Optical properties

We shall note that the international MKSA units have been explicitly used throughout the paper and the electric field of electromagnetic plane-waves in the form $E = E_0 \exp[j(\omega t - kx)]$ has been assumed, where $j = (-1)^{1/2}$ and ω and k are the circular frequency and the wavevector, respectively. Let us consider a plane-wave with the wavelength in vacuum λ impinging on an infinitely large non-structured metal film at normal incidence. The film has the thickness d and is located on top of an infinitely thick substrate with the refraction index n. The film is characterized by its complex permittivity $\varepsilon = \varepsilon_r \varepsilon_0$ and susceptibility $\mu = \mu_r \mu_0$. The reflection and transmission coefficients for the electric field are $r = E_r / E_i$ and $t = E_t / E_i$ where E_i, E_r and E_t are the amplitudes of the electric field in the incident wave, reflected wave and the wave propagating into the dielectric, respectively. The coefficients are connected by the following matrix equation [28]

$$\begin{bmatrix} 1+r \\ \frac{1}{Z_0}(1-r) \end{bmatrix} = \begin{bmatrix} \cosh(\Gamma d) & Z_M \sinh(\Gamma d) \\ \frac{1}{Z_M}\sinh(\Gamma d) & \cosh(\Gamma d) \end{bmatrix} \cdot \begin{bmatrix} t \\ \frac{n}{Z_0} t \end{bmatrix}, \tag{A1}$$

where $Z_0 = (\mu_0 / \varepsilon_0)^{1/2}$ is the impedance of vacuum, $Z_M = Z_0 (\mu_r / \varepsilon_r)^{1/2}$ is the surface impedance of the metal and Γ is the propagation constant in the metal

$$\Gamma = -j \frac{2\pi}{\lambda} \sqrt{\varepsilon_r \mu_r} \, . \tag{A2}$$

Based on energy conservation, the absorbance of the metal film can be written as

$$A = 1 - r r^* - n t t^* , \tag{A3}$$

where the asterisks stay for complex conjugate. The reflection and transmission coefficients r and t are solutions of (A1)

$$r = \frac{(1-n)\sqrt{\frac{\varepsilon_r}{\mu_r}}\cosh(\Gamma d) + (n - \frac{\varepsilon_r}{\mu_r})\sinh(\Gamma d)}{(1+n)\sqrt{\frac{\varepsilon_r}{\mu_r}}\cosh(\Gamma d) + (n + \frac{\varepsilon_r}{\mu_r})\sinh(\Gamma d)}$$

$$t = \frac{2\sqrt{\frac{\varepsilon_r}{\mu_r}}}{(1+n)\sqrt{\frac{\varepsilon_r}{\mu_r}}\cosh(\Gamma d) + (n + \frac{\varepsilon_r}{\mu_r})\sinh(\Gamma d)} \quad . \tag{A4}$$

For a thin metal film falling under the condition $|\Gamma d| << 1$ and consequently $d << \delta$, where $\delta = 1/\mathrm{Re}(\Gamma)$ is the skin depth, the expressions (A4) can be simplified to make the absorbance (A3) a function of impedances only

$$A = \frac{4 Z_0 \,\mathrm{Re}(Z_F)}{\left|Z_0 + (n+1) Z_F\right|^2}, \tag{A5}$$

where the impedance of the metal film $Z_F = Z_0(\mu_r/\varepsilon_r)^{1/2}(\Gamma d)^{-1} = Z_M(\Gamma d)^{-1}$. At frequencies well below the reciprocal electron scattering time and in the case of a "good" metal, i.e. a metal with large dc conductivity $\sigma > \omega\,\varepsilon_r\varepsilon_0$, the complex permittivity is almost imaginary $\varepsilon_r \approx \sigma\,(j\,\omega\,\varepsilon_0)^{-1}$. Then the film impedance becomes real and for $\mu_r = 1$ approaches the dc square resistance of the film $Z_F \approx R_S = (\sigma d)^{-1}$. The expression (A5) then reduces to the conventional form $A \approx 4\,Z_0\,R_S\,(Z_0 + (n+1)\,R_S)^{-2}$ that is commonly used for estimates of the absorbance of thin metal films. For a thin film made from a good metal deposited on a sapphire substrate the value of the square resistance $R_S \approx Z_0\,(n+1)^{-1} \approx 140\,\Omega$ maximizes the film absorbance.

B. Transport properties

According to the GL model, the upper critical magnetic field is connected with the superconducting coherence length ξ and the magnetic flux quantum $\Phi_0 = h\,(2e)^{-1}$ as

$$B_{C2}(T) = \frac{\Phi_0}{2\pi\,\xi(T)^2}\,. \tag{A6}$$

The exact microscopic relation between the GL coherence length $\xi(T)$ and the BCS coherence length $\xi_0 = \hbar v_F\left[\pi\,\Delta(0)\right]^{-1} = \mathrm{e}^{\gamma}\hbar v_F\left[\pi^2 k_B T_C\right]^{-1}$ (here $\gamma = 0.577$ is Euler's constant, $\Delta(0)$ the superconducting energy gap at $T = 0$ and v_F is the Fermi velocity) depends on the transport properties of the superconducting material. For dirty superconductors the GL coherence length in the vicinity of T_C is [29]

$$\xi(T) = \left(\frac{\pi^3}{24\,e^{\gamma}}\right)^{\frac{1}{2}}(\xi_0 l)^{\frac{1}{2}}\left(\frac{T_\mathrm{C} - T}{T_\mathrm{C}}\right)^{-\frac{1}{2}} \tag{A7}$$

After substituting this expression for $\xi(T)$ in Eq. (A6) and taking the derivative at $T = T_C$ one obtains $(dB_{C2}/dT) = -4k_B(\pi e D)^{-1}$ that gives the electron diffusivity in practical units displayed in Eq. 2.
A linear extrapolation of the measured $B_{C2}(T)$ down to $T = 0$ K certainly overestimates the real upper critical field at zero temperature. A more realistic value in the dirty limit is [30]

$$B_{C2}(0) = 0.69T_C\left[\frac{dB_{C2}(T)}{dT}\right]_{T=T_C}. \quad \text{(A8)}$$

The resulting upper critical fields of about 20 T or larger suggest that $B_{C2}(0)$ is further reduced due to spin paramagnetism and spin-orbit scattering [31]. The obtained value should thus be taken as the upper limit for $B_{C2}(0)$. With this $B_{C2}(0)$ the GL coherence length at $T = 0$ can be determined from (A6) but due to the uncertainty in $B_{C2}(0)$, this value is in turn a lower limit. However, because of the square-root dependence of ξ on B_{C2}, this should give a satisfactory estimate of the coherence length in our films.
The depairing critical current density in the GL model was shown to be $j_C(T) = \Phi_0\left[3^{3/2}\pi\mu_0\Lambda(T)^2\xi(T)\right]^{-1}$, where $\Lambda(T)$ is the effective magnetic penetration depth. Using the exact microscopic expressions for $\Lambda(T)$ in the dirty limit [29]

$$\Lambda(T)^2 = \frac{21\zeta(3)}{8\pi e^{\gamma}}\frac{\xi_0}{l}\frac{1}{\mu_0 e^2 v_F^2 N_0}\left(\frac{T_C - T}{T_C}\right)^{-1}, \quad \text{(A9)}$$

where N_0 is the electron density of states per one spin at the Fermi level and $\zeta(3) = 1.202$ and invoking the two-fluid temperature dependence of the depairing current density $j_C(T) = j_C(0)(1-t^2)(1-t^4)^{1/2}$, we derived the expression for $j_C(0)$ as a function of accessible parameters $j_C(0) = 2.26\,e\,N_0(k_B T_C)^{3/2}(D/\hbar)^{1/2}$. In practical units it reduces to Eq. 3 in Section II.

References

[1] V. Anant, A.J. Kerman, E.A. Dauler, J.K.W. Yang, K.M. Rosfjord, and K.K. Berggren, Optics Express **16**, 10750 (2008).
[2] Z. Wang, A. Kawakami, Y. Uzawa, and B. Komiyama, J. Appl. Phys. **79**, 7837 (1998).
[3] J.C. Villégier, N. Hadacek, S. Monso, B. Delaet, A. Rossy, P. Febvre, G. Lamura, and J.Y. Laval, IEEE Trans. Appl. Supercond. **11**, 68 (2001).
[4] J.R. Gao, M. Hajenius, F.D. Tichelaar, T.M. Klapwijk, B. Voronov, E. Grishin, G. Gol'tsman, C.A. Zorman, and M. Mehregany, Appl. Phys. Lett. **91**, 062504 (2007).
[5] R. Espiau de Lamaëstre, Ph. Odier, and J.C. Villégier, Appl. Phys. Lett. **91**, 232501 (2007).
[6] R. Sanjinés, M. Benkahoul, C.S. Sandu, P.E. Schmid, and F. Lévy, Thin Solid Films **494**, 190 (2006).

[7] S.P. Chockalingam, M. Chand, J. Jesudasan, V. Tripathi, and P. Raychaudhuri, Phys. Rev. **B 77**, 214503 (2008).
[8] K.E. Kornelsen, M. Dressel, J.E. Eldridge, M.J. Brett, and K.L. Westra, Phys. Rev. **B 44**, 11882 (1991).
[9] K. Il'in, M. Siegel, A. Engel, H. Bartolf, A. Schilling, A. Semenov, H.-W. Hübers, Journal of Low Temperature Physics **151**, 585 (2008).
[10] A. Engel, A. Semenov, H.-W. Hübers, K. Il'in, M. Siegel, Chapter 6, Electric Noise and Local Photon-Induced Nonequilibrium States, in New Frontiers in Superconductivity Research, Ed. by B.P. Martins, pp. 153-189, NOVA Publishers, 2006.
[11] H. Bartolf, A. Engel, L. Gómez and A. Schilling, Raith Applicaton Note (2008).
[12] K. Ilin, R. Schneider, D. Gerthsen, A. Engel, H. Bartolf, A. Schilling, A. Semenov, H.-W. Huebers, B. Freitag, and M. Siegel, Journal of Physics: Conference Series **97**, 012045 (2008).
[13] A. Darlinski and J. Halbritter, Surface and Interface Analysis **10**, 223 (1987).
[14] L.G. Aslamazov, A.I. Larkin, Phys. Lett. **26A**, 238 (1968).
[15] S. I. Park, T. H. Geballe, Physica **135B**, 108 (1985); S. Kubo, M. Asahi, M. Hikita, M. Igarashi, Appl. Phys. Lett. **44**, 2, 258, 1984.
[16] A Engel, H Bartolf, A Schilling, K Il'in, M Siegel, A Semenov, and H-W Hübers, Journal of Physics: Conference Series **97**, 012152 (2008).
[17] R. Romestain, B. Delaet, P. Renaud-Goud, I. Wang, C. Jorel, J.C. Villégier, and J.Ph. Poizat, New Journal of Physics **6**, 129 (2004).
[18] S.P. Chockalingam, M. Chand, A. Kamlapure, J. Jesudasan, A. Mishra, V. Tripathi, and P. Raychaudhuri, Phys. Rev. **B 79**, 094509 (2009).
[19] I.V. Roshchin, A.C. Abeyta, L.H. Greene, T.A. Tanzer, J.F. Dorsten, P.W. Bohn, S-W. Han, P.F. Miceli, and J.F. Klem, Phys. Rev. **B 66**, 134530 (2002).
[20] M.P. Mathur, D.W. Deis, and J.R. Gavaler, J. Appl. Phys. **43**, 3158 (1972).
[21] W. Słysz, M. Węgrzecki, J. Bar, P. Grabiec, M. Górska, V. Zwiller, C. Latta, P. Bohi, I. Milostnaya, O. Minaeva, A. Antipov, O. Okunev, A. Korneev, K. Smirnov, B. Voronov, N. Kaurova, G. Gol'tsman, A. Pearlman, A. Gross, I. Komissarov, A. Verevkin, and Roman Sobolewski, Appl. Phys. Lett. **88**, 26113 (2006).
[22] P. Yeh, Optics Communications **26**, 289 (1978).
[23] A. Christ, T. Zentgraf, J. Kuhl, S. G. Tikhodeev, N. A. Gippius, and H. Giessen, Phys. Rev. **B 70**, 125113 (2004).
[24] A.D. Semenov, P. Haas, B. Günther, H -W. Hübers, K. Il'in, M. Siegel, A. Kirste, J. Beyer, D. Drung, T. Schurig and A. Smirnov, Superconductor Science and Technology **20**, 919 (2007).
[25] S. N. Dorenbos, E. M. Reiger, N. Akopian, U. Perinetti, V. Zwiller, T. Zijlstra, and T. M. Klapwijk, Appl. Phys. Lett. **93**, 161102 (2008).
[26] A. Semenov, A. Engel, H.-W. Hübers, K. Il'in, M. Siegel, The European Phys. Journal **B 47**, 495 (2005).
[27] X.J. Yu and H.S. Kwok, Journal of Applied Physics **93**, 4407 (2003).
[28] Eugene Hecht, Optics, Addison-Wesley Publishing Company, Inc., 1987
[29] Superconductivity, R.D. Parks – editor, Marcel Dekker, Inc., New York, 1969 (Chapter 6). For closed expressions in EM units see T.P. Orlando, E.J. McNiff, Jr.; S. Foner, and M.R. Beasley, Phis. Rev. **B 19**, 4545 (1979). Note the misprint on the page 4560 in the expression for the slope of the second critical magnetic field near T_C in the dirty limit. There should be $-(\mathrm{d}H_{C2}/\mathrm{d}T)^{\mathrm{d}} = 24\, e^{\gamma}\, \hbar\, c\, (2\, e\, \pi^3\, \xi_0\, l_{\mathrm{tr}}\, T_C)^{-1}$. Closed expressions can be also found in Type II Superconductivity, D. Saint.James, G. Sarma, and E.J. Thomas, Pergamon Press, 1969.
[30] E. Helfand and N.R. Werthamer, Phys. Rev. **147**, 288 (1966).
[31] N.R. Werthamer, E. Hefland, and P.C. Hohenberg, Phys. Rev. **147**, 295 (1966).

Table 1

Sample #	[1] d	T_C	$R_S(295)$	$\mathrm{Re}(Z_F)$	RRR	D	$\rho_n(T>T_C)$	τ	l	ω_p	$j_C(0)$	N_0
	nm	K	Ω	Ω		$\mathrm{cm}^2\,\mathrm{sec}^{-1}$	μΩ m	fsec	nm	$10^{15}\,\mathrm{rad\,sec}^{-1}$	MA cm^{-2}	$10^{47}\ \mathrm{J}^{-1}\ \mathrm{m}^{-3}$
308	3.2	9.87	707	490	0.850	[2] 0.510	2.66	2.16	0.58	13.46	2.92	0.73
350	3.3	10.84	688		0.823	0.510	2.76				3.94	0.86
352	3.9	11.84	572		0.824	0.570	2.71				6.04	1.09
351	4.3	12.44	478		0.856	0.561	2.40				7.32	1.24
349	5.1	13.23	341		0.910	0.582	1.91				8.29	1.25
206	5.3	11.54	261		0.950	0.664	1.46				7.94	1.38
73	5.6	12.99	280		0.922	0.587	1.70				8.30	1.29
303	5.8	13.50	265	230	0.930	[2] 0.587	1.65	3.54	0.79	12.45	9.51	1.39
207	6.7	13.47	145		1.001	0.646	0.97				10.61	1.55
173	8	13.99	191		0.979	0.599	1.56				11.50	1.58
305	8.3	14.40	165	148	0.950	[2] 0.599	1.44	3.53	0.80	12.96	11.35	1.49
307	11.7	15.20	105	96	0.980	[2] 0.599	1.25	3.48	0.79	13.55	13.46	1.63
281	14.4	15.25	84	72	1.033	0.598	1.17	3.86	0.83	14.66	13.30	1.60

Table 1. (Color online) Transport and optical properties of studied NbN films. $R_S(295)$ - square resistance at room temperature; RRR - the residual resistance ratio at 295 K and 20 K; $\mathrm{Re}(Z_F)$ – the real part of the optical film impedance for a wavelength of $5\,\mu\mathrm{m}$ as derived from ellipsometry data; l - electron mean free path. [1] The thickness that appears in the table is the total thickness including NbN and Nb_2O_5 layers. [2] Values were obtained by interpolating between adjacent measured values. Shaded lines mark films which were grown with nitrogen deficiency.

Table 2

Sample #	d	ε_{r0}	Ω_{01}	Ω_{S1}	Ω_{D1}	Ω_{02}	Ω_{S2}	Ω_{D2}
308	3.2	2.58	9.58	21.73	7.08	1.32	6.83	2.42
303	5.8	2.58	9.58	21.73	7.08	1.68	8.85	3.03
305	8.3	2.58	9.58	21.73	7.08	1.78	8.85	3.27
307	12	2.58	9.58	21.73	7.08	1.89	7.80	3.27
281	15	2.58	9.58	21.73	7.08	2.26	4.74	2.95

Table 2. Parameters of the single oscillators, which were used to obtain the best fit of the experimental data with equation (1). Thicknesses are in nanometers and oscillator frequencies are in units of $10^{15}\,\mathrm{rad\,sec^{-1}}$.

Table 3

Sample #	T_C	d	w	$\rho_n(T > T_C)$	R_H	n_e	$k_F\,l$
	K	nm	μm	μΩ m	10^{-11} m^3C^{-1}	10^{29} m^{-3}	
376	10.72	3.2	10	3.01	-2.406	2.59	2.61
375	14.02	6	10	1.41	-4.961	1.26	5.56
377	15.17	12	5	1.09	-4.951	1.26	5.65

Table 3. Hall coefficients R_H, free-electron concentrations n_e and the Ioffe-Regel parameters $k_F\,l$ for three films which were specially prepared for Hall measurements.

Figure captures

Figure 1. (Color online) HRTEM micrograph of the film (a), the AFM picture of one edge of the grating (b) and the AFM profile of the grating made at right angles to the grating wires (c). The line-width and the pitch of the grating are 174 nm and 258 nm, respectively. HRTEM imaging gives an NbN film thickness of about 5 ± 1 nm which is in good agreement with the total thickness of ≈6 nm measured by AFM.

Figure 2. (Color online) Superconducting transition temperature (closed symbols) and resistivity at $T \geq T_C$ (open symbols) for NbN films on sapphire as a function of film thickness. Circles mark the resistivity of two films (#206 and #207) grown with nitrogen deficiency.

Figure 3. (Color online) Real ε_1 and imaginary ε_2 parts of the relative dielectric constant $\varepsilon_r = \varepsilon_1 + j\varepsilon_2$ of a few NbN films with different thicknesses. Film thickness is specified in the legend. Data were obtained by ellipsometry.

Figure 4. (Color online) Absorbance of non-structured NbN films with different thicknesses. Thicknesses are specified in the legend. Inset: Real (solid line) and imaginary (dotted line) parts of the impedance for the 5.6 nm thick film.

Figure 5. (Color online) Temperature dependence of the upper critical magnetic field. Legend specifies the film thickness. Solid lines represent linear approximations of the experimental data for each thickness as described in the text.

Figure 6. (Color online) Electron density of states for films with different thicknesses evaluated according to (3) from critical current measurements.

Figure 7. (Color online) Hall voltages for three films of different thicknesses as a function of magnetic induction. Longitudinal voltage components have been subtracted. The temperature was kept constant at 50 K. Solid lines are linear least-square fits to the data from which the Hall coefficient R_H has been derived.

Figure 8. (Color online) Computed absorbance of gratings with different filling factors for polarization parallel (s-pol) and perpendicular (p-pol) to the wires. Wires are 90 nm wide strips from 5.6 nm thick film. Filling factors are specified in the legend.

Figure 9. (Color online) Ratio of photon count rates for light polarized parallel and perpendicular to meander lines. Symbols represent experimental data for two meanders both covering the area 4×4 μm^2 with the line width, thickness and filling factor 90 nm/4.8 nm/50% (triangles) and 80 nm/4.3 nm/47% (squares), respectively. Solid lines show the extinction ratio computed for these gratings with FEKO.

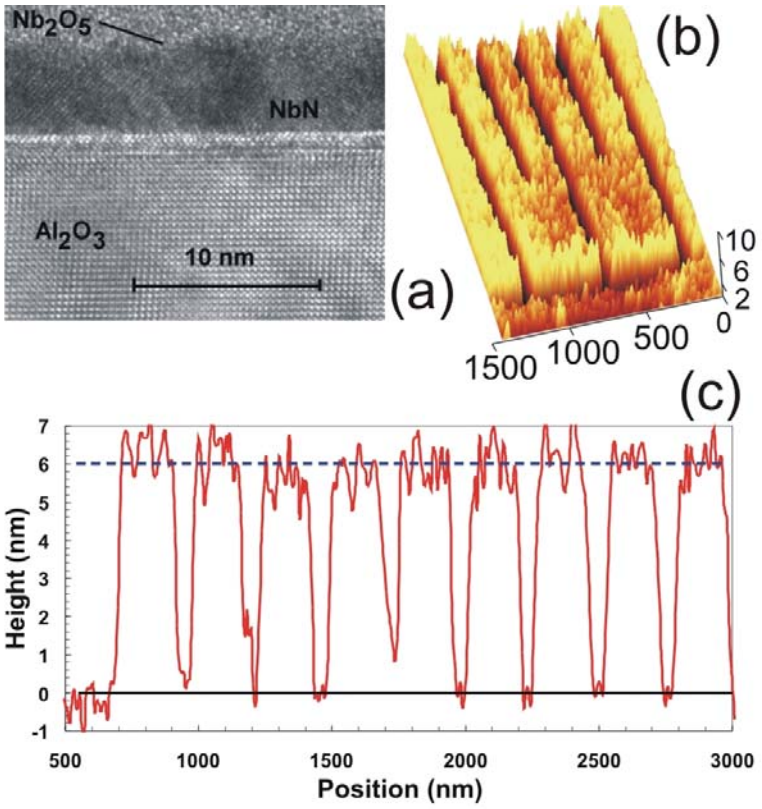
Nb_2O_5
NbN
Al_2O_3
10 nm
(a)
(b)
10
6
2
0
1500
1000
500
(c)
Height (nm)
Position (nm)

Fig. 1

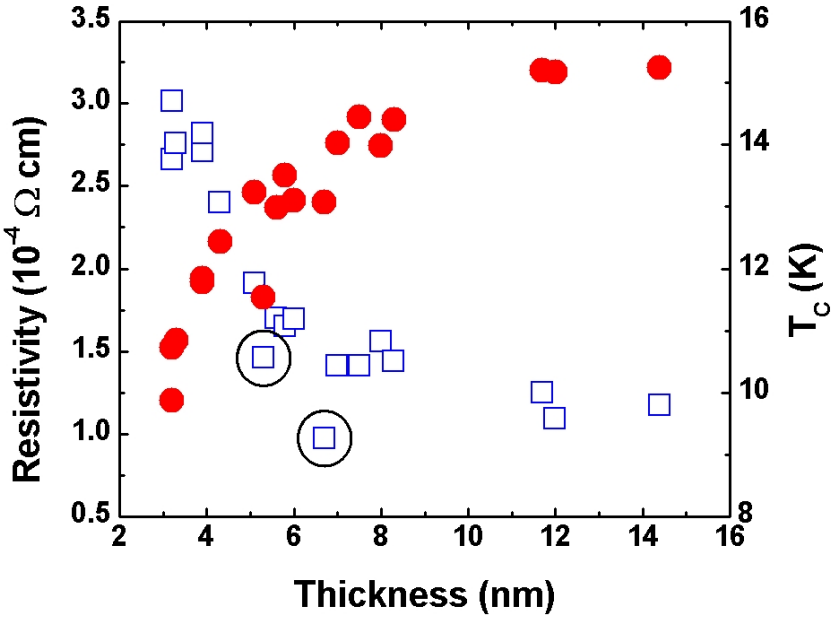
Resistivity (10^{-4} Ω cm)
T_c (K)
Thickness (nm)

Fig. 2

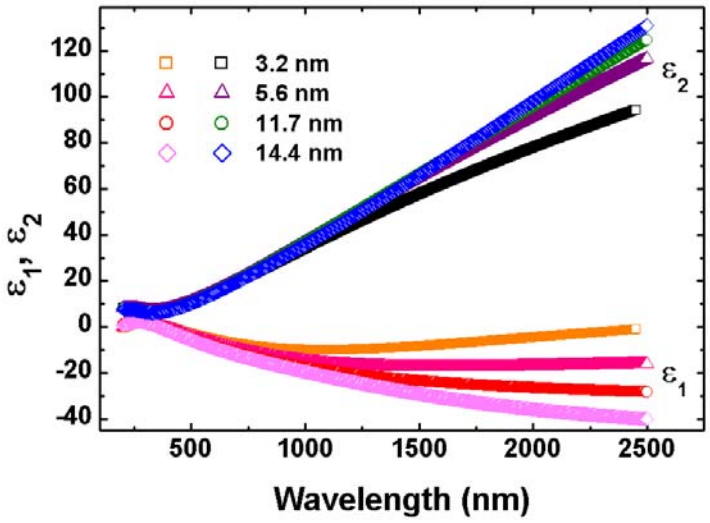
3.2 nm
5.6 nm
11.7 nm
14.4 nm
ε2
ε1
ε1, ε2
Wavelength (nm)

Fig. 3

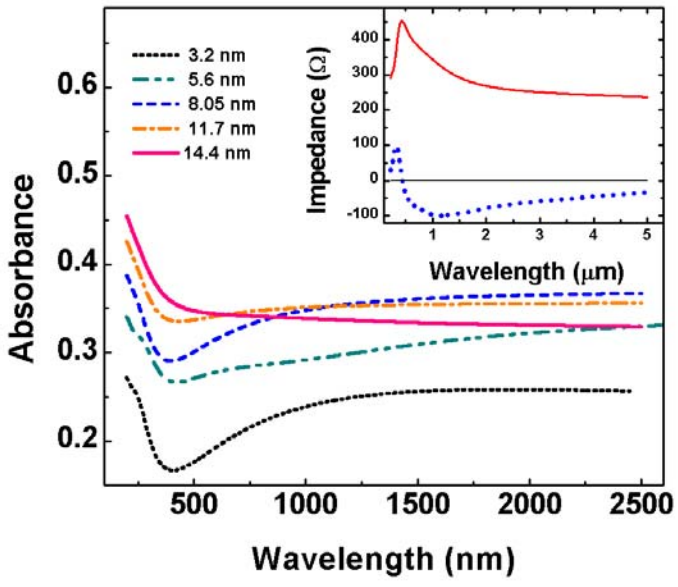
3.2 nm
5.6 nm
8.05 nm
11.7 nm
14.4 nm
Impedance (Ω)
Wavelength (μm)
Absorbance
Wavelength (nm)

Fig. 4

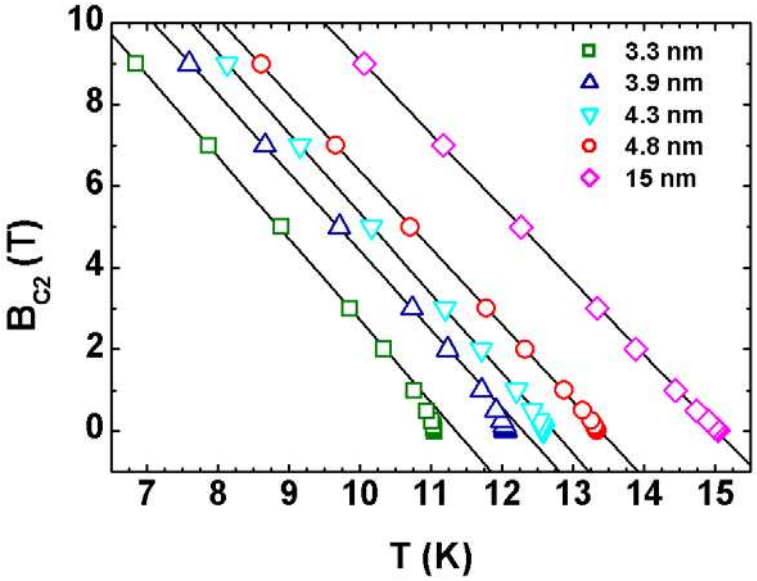
3.3 nm
3.9 nm
4.3 nm
4.8 nm
15 nm
B_{c2} (T)
T (K)

Fig. 5

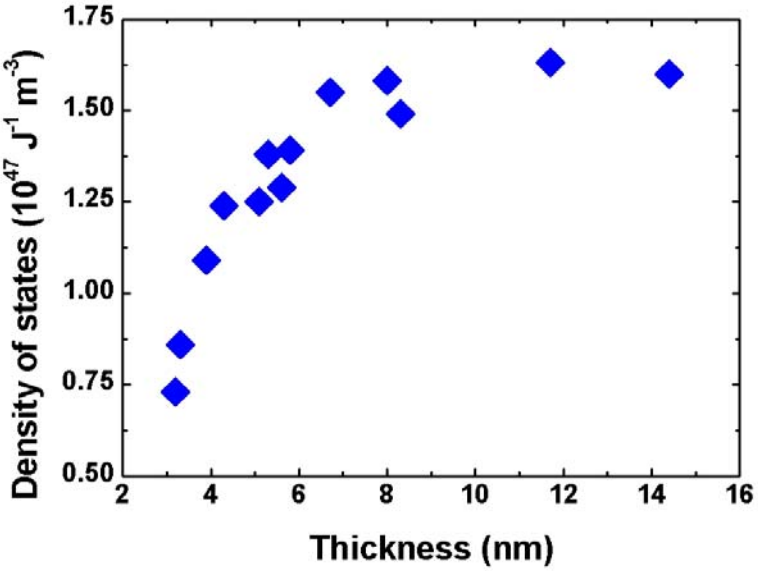
Density of states (10^{47} J^{-1} m^{-3})
Thickness (nm)

Fig. 6

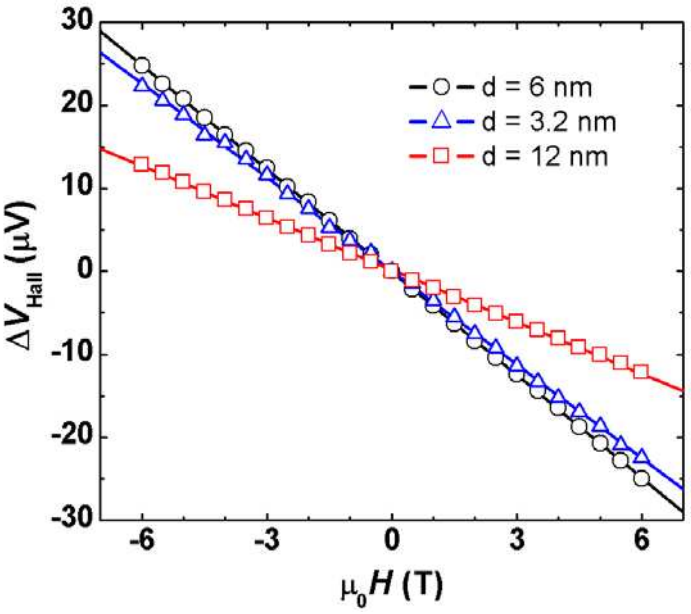
d = 6 nm
d = 3.2 nm
d = 12 nm
ΔV_{Hall} (μV)
$\mu_0 H$ (T)

Fig. 7

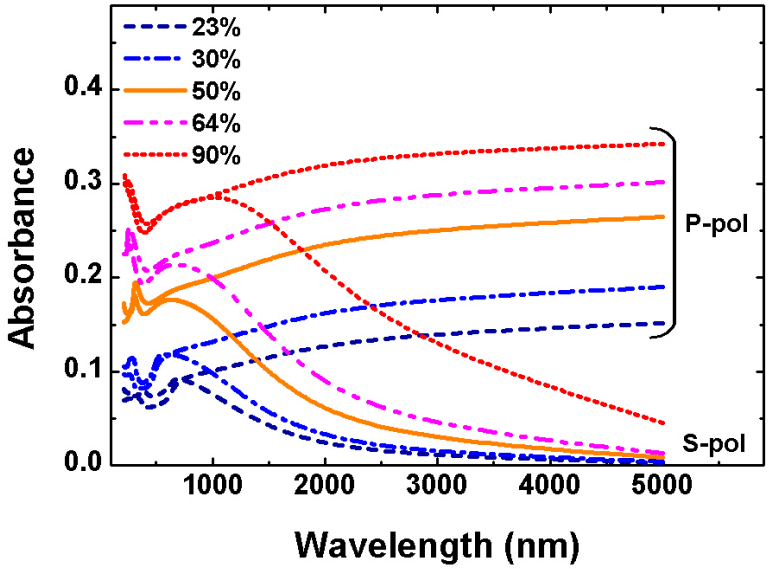
23%
30%
50%
64%
90%
P-pol
S-pol
Absorbance
Wavelength (nm)

Fig. 8

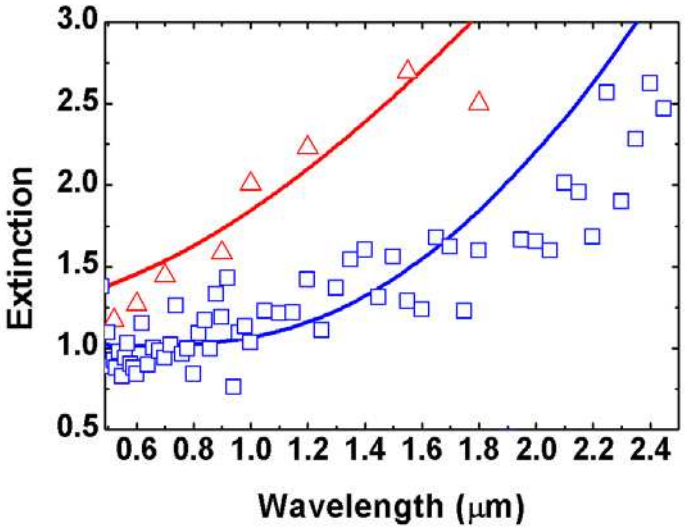
Extinction
3.0
2.5
2.0
1.5
1.0
0.5
0.6 0.8 1.0 1.2 1.4 1.6 1.8 2.0 2.2 2.4
Wavelength (μm)

Fig. 9